CHAPTER I

CORRELATING MR RELAXATION MEASUREMENTS WITH PROTEOMIC INFORMATION PROVIDED BY MALDI USING C6 GLIOMA TUMOR MODEL

Introduction

The premise of this work is to understand the contrast variations seen in MRI in light of the proteomic composition of tissue. Magnetic resonance imaging (MRI) is now widely used as a primary medical imaging method to visualize the internal structure and function of different tissues in human body. The contrast seen in MR images is inherently manipulated by spatial variations in tissue NMR properties, such as relaxation times, tissue microenvironment, water density, and water diffusion. However, what macromolecular components may be correlated with the contrast changes we seen in MR is not well understood. Here we explore whether variations in MR properties could be correlated with corresponding tissue macro-molecular changes as measured by matrix-assisted laser desorption/ionization imaging mass spectrometry (MALDI IMS). By doing so, we aim to understand factors that affect the relaxation at the molecular level.

MRI has become a part of clinical standard of care in a variety of disease states. Areas of clinical interest in MRI includes central nervous system [1-3], cardiovascular [4-6], musculoskeletal system[7-9] and so on. The majority of clinical diagnoses using MRI rely on the intrinsic contrast between pathological and healthy tissue. For example, in brain tumors, there is an increase in the

water concentration, as well as an increase in the relaxation times. T2-weighted sequence will show the tumor as an area of higher signal intensity than the surrounding tissue. Other disease such as Parkinson and Alzheimer could also be detected by MRI, where the deposition of irons in the putamen caused the decrease of T2 of the surrounding water thereby resulting in a signal intensity reduction on T2 weighted sequences. Besides, MRI signal is very sensitive to a number of other parameters, such as the diffusion coefficient of water, where it has been found to be an extremely sensitive parameter related to the extent of stroke in the very early stages after the episode. MRI's multi-planar capabilities and sensitivity to tissue differentiation makes it the procedure choice of detecting abnormalities or lesions in most parts of the body. The improvement of MR image contrast is thereby of great importance and the study of factors that affect relaxation has great potential value.

Background

Relaxation Theory

Relaxation is termed as the process by which a spin system regains thermal equilibrium after perturbation by RF pulse, through interaction with the thermal molecular environment. Theoretically, samples placed in magnetic field undisturbed for a long time (on the order of seconds) will reach a state of thermal equilibrium, where all the coherence between the spins are absent and the populations are governed by the Boltzmann distribution. This equilibrium reached in magnetic field could be perturbed by a radio frequency pulse that is dependent upon the static magnetic field and the nuclei of observation.

Relaxation of nuclear spins requires a microscopic mechanism for a nucleus to change orientation with respect to the applied magnetic field and/or interchange energy with the surroundings (called the lattice). The most common mechanism is the magnetic dipole-dipole interaction between the magnetic moment of a nucleus and the magnetic moment of another nucleus or other entity (electron, atom, ion, molecule). Relative motion of a pair of magnetic dipoles due to thermal motion causes fluctuating interaction energies. According to quantum mechanics, time-dependent interaction energies cause transitions between the nuclear spin states which result in nuclear spin relaxation. The application of time-dependent perturbation theory in quantum mechanics shows that the relaxation rates (and times) depend on spectral density functions which are the Fourier transforms of the auto-correlation function of the fluctuating magnetic dipole interactions [10].

There are two typical relaxation types, spin-lattice relaxation (which also termed longitudinal relaxation) and spin-spin relaxation (which also termed transverse relaxation). The former is concerned with the movement of spin populations back to their Boltzmann distribution while the latter one describes the decay of coherence of the spins. For an ensemble of isolated spins-1/2, there are two time constants for the relaxation process, T1 for the spin-lattice relaxation and T2 for the spin-spin relaxation.

Based on the relaxation theory talked above, these two time constants could be written in terms of the transition rates to obtain the following expressions [11].

$$R_1^H(^1H,^1H) = \frac{1}{T_1} = \frac{3}{10} b^2 \{\Im(\omega_H) + 4\Im(2\omega_H)\} \qquad \text{(Equation 1)}$$

$$R_2^H(^1H,^1H) = \frac{1}{T_2} = \frac{3}{20} b^2 \{3\Im(0) + 5\Im(\omega_H) + 2\Im(2\omega_H)\} \qquad \text{(Equation 2)}$$

Where $\Im(0)$ is the spectral density of the dipole-dipole couplings at zero frequency, $\Im(\omega_H)$ is the spectral density of the dipole-dipole couplings at the Larmor frequency ω_H , and b is the dipole-dipole coupling constant.

Experimentally, when a sample of magnetically active nuclei is placed in a static magnetic field, a polarization or macroscopic magnetization will be produced within the sample. This induced magnetization does not arise instantaneously, but instead accumulates at an exponential rate. For the longitudinal relaxation time T1, if we tip the macroscopic magnetization away from the static field axis by applying a resonant RF irradiation, the recovery of the magnetization to the original state could be characterized by this time constant,

$$\frac{M_z(\tau) - M_z(\infty)}{M_z(0) - M_z(\infty)} = e^{-\tau/T_1} \qquad \text{(Equation 3)}$$

Where $M_z(0)$ is the magnetization immediately following the perturbation, $M_z(\infty)$ is the fully restored equilibrium magnetization and $M(\tau)$ is the magnetization at an interval τ ,following the perturbation. Manipulating with the equation 3 above, we will get

$$M_z(\tau) = M_z(\infty) + (M_z(0) - M_z(\infty))e^{-\tau/T_1} \qquad \text{(Equation 4)}$$

If the macroscopic magnetization was tilted into the transverse plane, then $M_z(0) = 0$, and the recovery is simply

$$M_z(\tau) = M_z(\infty)(1 - e^{-\tau/T_1}) \quad \text{(Equation 5)}$$

The transverse (spin-spin) relaxation time T2, is the time constant characterize the de-correlation between the different spins in the transverse plane. The decay should follow the expression below:

$$M_{xy}(\tau) = M_{xy}(0)e^{-\tau/T_2} \quad \text{(Equation 6)}$$

Therefore, if a $\pi/2$ RF pulse is applied at interval time TR where any previous transverse magnetization has decayed away due to the spin-spin effect and only the longitudinal magnetization corresponding to equation 5 remains to be rotated into the transverse plane, the signal should be proportional to the magnitude of the transverse magnetization given by

$$M_z(T_E) = M_z(\infty)(1 - e^{-T_R/T_1})e^{-T_E/T_2} \quad \text{(Equation 7)}$$

Where T_E is the echo time where the signal data are instantaneous sampled. A three-parameter fit to the equation 7 will give back the estimation of both T1 and T2. The differences in measured relaxation rates provide the basis for contrast changes in different tissues when imaged by MRI. However, to date, we still lack adequate explanations on processes and factors that caused the differences in relaxation rates in different tissues at the macromolecular level. Therefore, there

is considerable potential value in elucidating the specific biophysical components that may affect the relaxation rates and thereby the *in vivo* contrast variations.

Theoretical Model

We have derived our own theoretical model to predict the potential relationship between relaxation measurements and tissue macromolecular profile. Mathematically, suppose within a voxel there is a total mass of water distributed between bounded and free fractions,

$$f_b = \frac{hm_p}{hm_p + m_f} \qquad \text{(Equation 8)}$$

where f_b is the fraction of bound/total water, h is the hydration water per gram protein, m_p and m_f are the amount of protein and free water within that voxel. In fast exchange,

$$R_1 = f_b R_b + f_f R_f = f_b(R_b - R_f) + R_f = f_b \Delta R_{bf} + R_f \qquad \text{(Equation 9)}$$

$f_f = 1 - f_b$ is the fraction of free/total water and R_f is the relaxation rate for free water. In any case,

$$R_1 = \Delta R_{bf} \frac{hm_p}{hm_p + m_f} + R_f \qquad \text{(Equation 10)}$$

So that,

$$R_1 - R_f \approx \Delta R_{bf} \frac{hm_p}{M_0}, (M_0 = \alpha h m_p + m_f) \qquad \text{(Equation 11)}$$

Assuming ΔR_{bf} and h are constants, M_0 is also constant for a given voxel with certain type and amount of sample. The relaxation rate for a given sample within a voxel should thereby be proportional to the amount of the tissue within that voxel.

$$R_1 - R_f \approx \frac{m_p}{M_0} \qquad \text{(Equation 12)}$$

This relationship could be extended to transverse relaxation rate as well.

There has been some work on relating the changes in MR relaxation to biophysical parameters in controlled studies. For example, Koenig has found that the high relaxation rate of white matter relative to gray matter in the adult brain is mainly due to the additional relaxation pathway in white matter provided by cross-relaxation at the water/myelin interface [12]. Damon and Gregory showed that the R2 decreases in exercising muscle could be explained by pH decreases and apparent intracellular volume increases [13]. Fenich et al presented a study on evaluation of multiple relaxation components from water protons in biological tissue [14]. Virta et al studied the effect of molecular weight, concentration and

structure on the rotating frame relaxation rate for several proteins using resonance spin-lock technique[15].

However, to date, a comprehensive examination of relaxation in light of tissue proteomics in situ has not been performed. The question of how, at the molecular and cellular level, factors and processes modulate the magnetic resonance signal remains. There are no models that predict quantitatively how normal tissue turns into diseased tissue, also less do we comprehend in detail why signal from same normal tissue are different.

Matrix-Assisted Laser Desorption Time-of-Flight Mass Spectrometry

We are interested in investigating the relationship between MR relaxation measurements and tissue proteomics using a relatively new tissue imaging technique called matrix assisted laser desorption/ionization imaging mass spectrometry (MALDI IMS). MALDI IMS is an extension of traditional MALDI mass spectrometry (MALDI MS) [16,17,18]. it is a soft ionization technique used in mass spectrometry, allowing the analysis of bio-molecules and large organic molecules, which tend to be fragile and fragment when ionized by more conventional ionization methods. The ionization is triggered by a laser beam. A

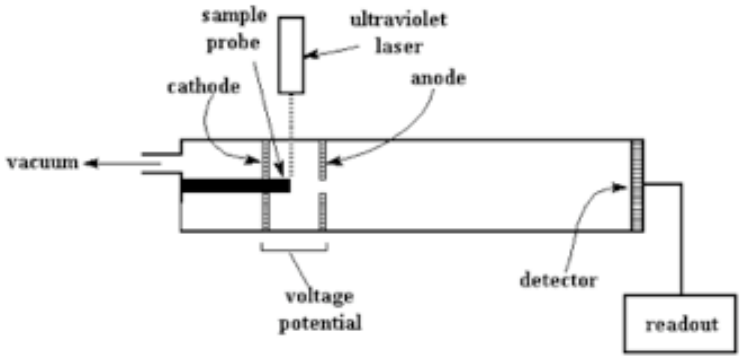

Figure 1. Diagram of a MALDI apparatus. (Creel H., Trends in Polym. Sci., 1993, 1(11), 336-342)

matrix is used to protect the bio-molecules from being destroyed by direct laser energy irradiation and to facilitate vaporization and ionization. A simplified diagram of a MALDI MS apparatus is shown in Figure 1.

MALDI IMS has been employed as an imaging technology in a wide variety of applications from the analysis of small molecules such as drugs and endogenous metabolites to macromolecules such as high molecular weight proteins. It has been successfully used to map different anatomic substructures of a mouse brain consisting of normal and tumor bearing regions [19]. Also, detection of pharmaceutical compounds in tissue by MALDI IMS was reported by Troendle et al. [20] and was further extended by Reyzer et al. to the imaging of anticancer drug and associated protein changes in tumor tissue from dosed mouse [21]. Groseclose et al developed a novel method for on-tissue identification of proteins in spatially discrete regions using tryptic digestion followed by MALDI IMS with MS/MS analysis [22]. Khatib-Shahidi et al performed a direct molecular analysis of whole-body animal tissue sections using MALDI IMS [23]. Andersson et al

performed a study to make 3D volume reconstructions of MALDI IMS data applied to the rat brain [24]. Cornett et al. developed a new approach to integrate the cellular specificity of histology, the accuracy and reproducibility of robotic liquid dispensing and the speed and objectivity of automated spectra acquisition. Their methods could improve the cellular specificity, and analysis throughput of protein profiles obtained by MALDI IMS analysis [25]. In these reports, it was shown that the MALDI IMS process could be rasterized across a tissue section generating an image where each pixel encoded the proteomic profile of the tissue at that spatial location, hence MALDI imaging mass spectrometry.

To sum up, the huge advantage of MALDI IMS is that it combines the parallel, high throughput molecular analysis with location specific information for the characterization of protein distribution directly from thin sections of intact biological tissue. Therefore, unlike other proteomic strategies like 2-D gel electrophoresis and LC-MS/MS analysis, MALDI IMS could preserve the spatial information of the tissue and highlight the small differences between regions of cells in tissue, consequently, reliably combine protein data with specific cellular regions within the tissue.

Data Analysis

By co-registering MALDI IMS data with MR, we can begin to investigate the spatial relationships between MR measurements and tissue macromolecular content. We have developed methods to acquire high signal-to-noise ratio MR

measurements on a rat head and generated the parametric maps along with it. After the imaging, corresponding proteomic profile of sections of interest for the rat head were acquired using MALDI technique. These two datasets were then registered together using well developed in house co-registration methods. Developments of this registration method have been addressed previously [26-36], here we will only focusing on the correlation analysis on the registered volume.

In all, our overall aim of this project is to attempt to understand the factors and processes that affect the MR signals in terms of macromolecular changes in tissue. We hypothesize that there will be correlated changes in MRI relaxation measurements when examined with corresponding protein profiles in the MALDI IMS data. In the following sections, we will describe our experimental design to test this hypothesis as well as results from our analysis of co-registered MALDI IMS data.

Methods

We examined co-registered MALDI IMS and MRI data in a rat model of brain cancer. In the following section we will outline the methods used to prepare the animal, our imaging techniques, and the processing techniques used to generate the co-registered correlation data.

Animal Model and Preparation

C6 glioma model male Wistar rats with an average weight of 250g were used. C6 glioma rat is widely used as an experimental model system for study of glioblastoma growth, invasion and metastasis [37]. Tumors grown from cells transplanted in rats have characteristics closer to natural glioblastomas than tumors grown in other rat strains. Glioblastoma multiforme (GBM) is the most common aggressive glioma resistant to therapeutic interventions. When injected into the brain of neonatal rats, C6 glioma cell line rapidly proliferated in the brain and is morphologically similar to GBM. Implantation models have been developed using Wistar Sprague-Dawley and Long-Evans rats. Due to their high affinity for the endothelial basement membrane, the C6 cells grow preferentially around blood vessels and invade the surrounding brain tissue through the release of proteolytic enzymes that generate micropockets which degrade the extracelluar matrix [37].

For the C6 rat model we used here, animals were anesthetized using a 2%98% isoflurane/oxygen mixture before the inoculation. 10^5 glioblastoma cells were then injected into the right side of the brain using a 10-mL gastight syringe, approximately 1 mm anterior and 2 mm lateral to the bregma with a depth of 3 mm relative o the dural surface.

MR Acquisition

Fourteen to sixteen days after the injection, the rats were imaged using a 9.4T MR spectrometer (Varian, Inc.). To minimize motion during scanning, the rat was

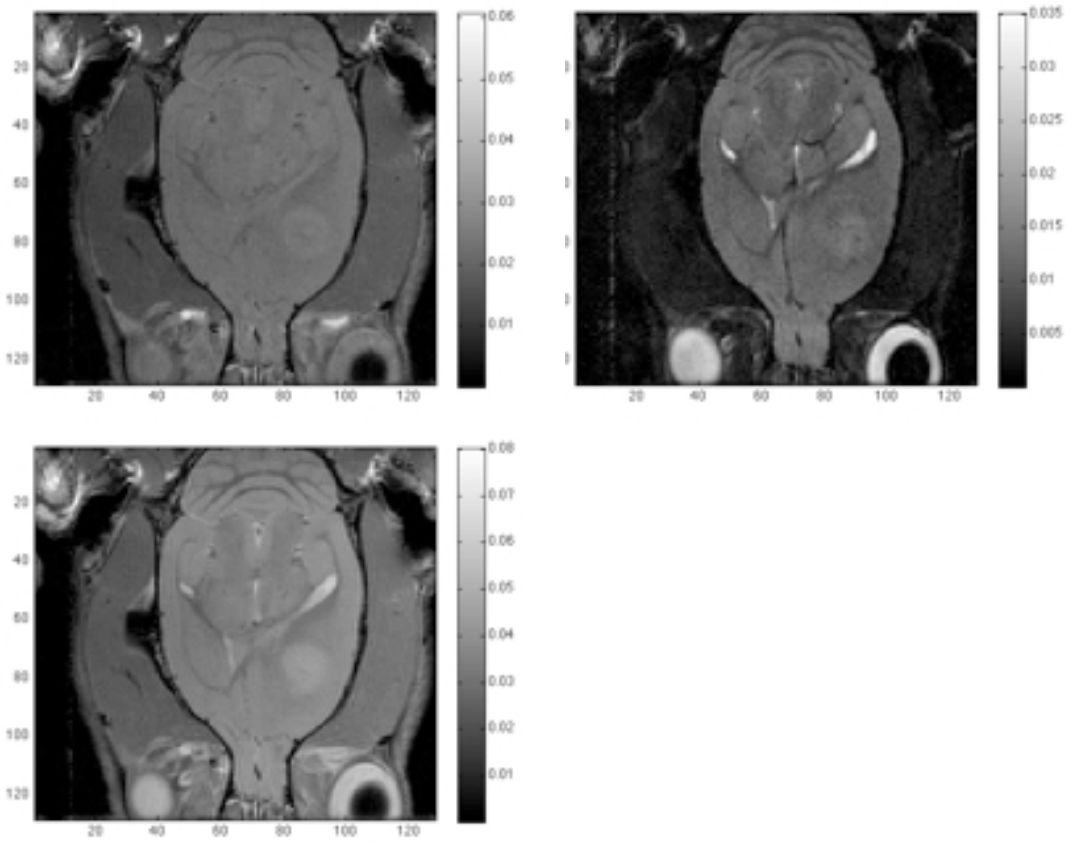

Figure 2. Images of Tumor rat brain under different TR/TE. The top left one has TR/TE = 2000/10 msec. Top right one has TR/TE = 8000/10 msec. Lower left one has TR/TE = 2000/45 msec. All 3 slices have a thickness of 0.5mm and are at the position of 12th in 25.

anesthetized with a gaseous 2%98% isoflurane/oxygen mixture and restricted using a custom stereotactic holder. A three-dimensional (3D) gradient-echo pulse sequence (TR=25msec, TE=4msec, Flip Angle=20 degree, Matrix =192x192x192, Field of View = 38.4x25.6x25.6m) was used to acquire a high resolution volume of the entire rat head. A multi-slice T2-weighted spin-echo pulse sequence with a variety of TR/TE combinations was used to acquire weighted images of the brain (TR = 8000/2000 msec, TE =10/45msec, # of slice =27, NEX=4, slice thickness = 05mm FOV=25.6mm x 30.0mm, matrix =

128x128). Figure 2 shows examples of tumor rat head MR images at 9.4T under different TR/TE combinations. Parametric maps of T1, T2, and M0 were generated in MATLAB using a non-linearly fitting method (i.e. the Nelder-Mead Simplex Optimization via 'fminsearch' function) (Mathworks, Inc.) to the following function:

$$S(x) = M_0(1 - e^{-TR/T_1})e^{-TE/T_2} \quad \text{(Equation 13)}$$

Where S(x) is the measurements for voxel x from weighted image, TR is the repetition time, and TE is the echo time. For each animal, a total of 81 parametric maps were derived.

MALDI Acquisition

Immediately after MR imaging, the rat was exsanguinated and perfused with saline. The decapitated rat head was flash frozen using dry-ice/hexane bath for 1~2 minutes. The frozen head was stored in a -80 degree Farenheit refrigerator to minimize the proteolytic degradation. The frozen rat head was then sectioned coronally using a cryomicrotome (Leica Microsystems, Inc.) at a section thickness of 15 um. Digital photographs of the blockface were acquired for alternating sections (i.e. every 30 um) during the sectioning process with a stationary digital camera that was rigidly attached to the microtome. The blockface images were then used to reconstruct the blockface volume, which was used as an intermediate reference frame during the co-registration [38].

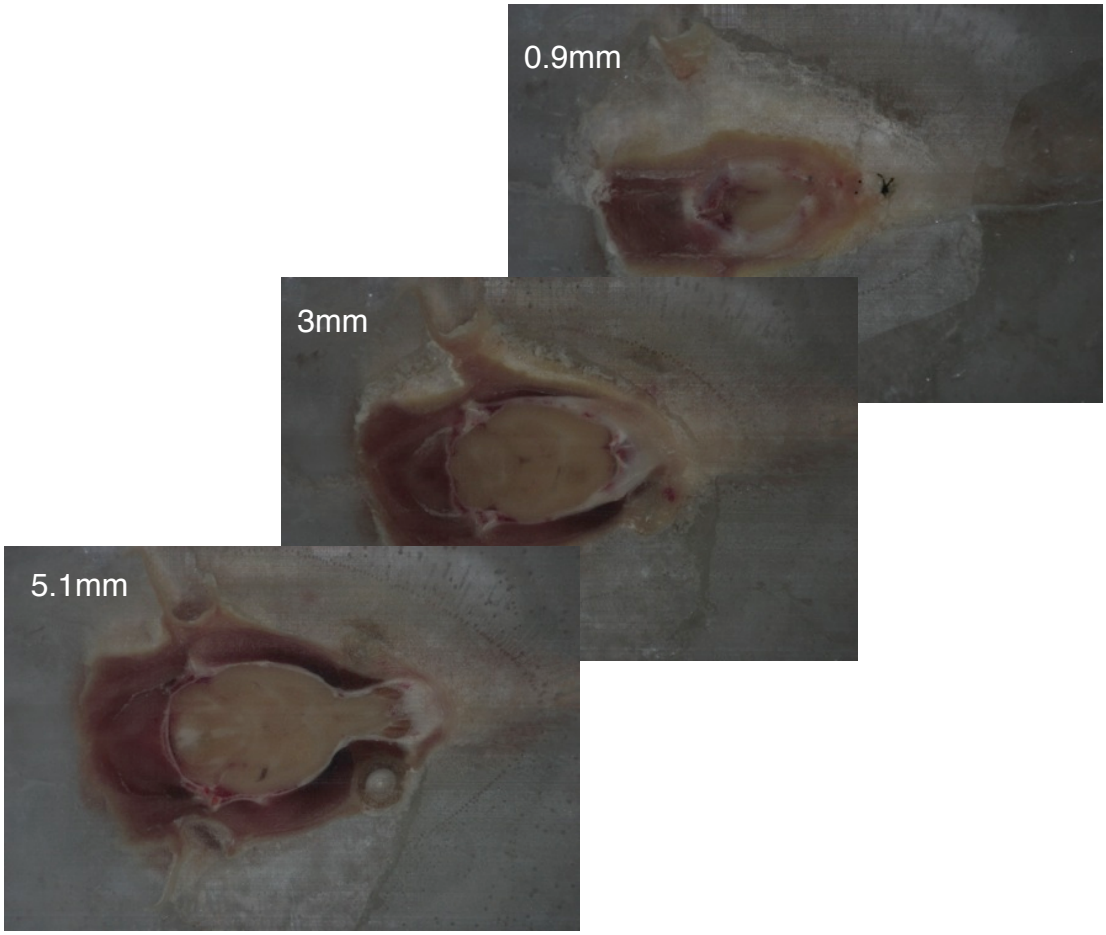

Figure 3. Examples of blockface images for a control rat at different depth.

Sections approximately 5mm deep in the brain (relative to the dorsal side of the a nimal) for MALDI were collected every 150 um, and were transferred to glass slides via photo-active tape-transfer protocol(Vibratome, Inc.).

The collected MALDI slides were then de-hydrated, spotted with a matrix solution of 20 mg/mL sinapinic acid prepared in 50% acetonitrile and 0.1% trifluoroacetic acid, and then irradiated using laser energy. The ionized macromolecules were recorded at a in-plane resolution of 200 um using time-of-flight (TOF) mass spectrometry techniques, yielding an image where each pixel contained a

spectrum of tissue macromolecules. Each MALDI image has 121x217 points

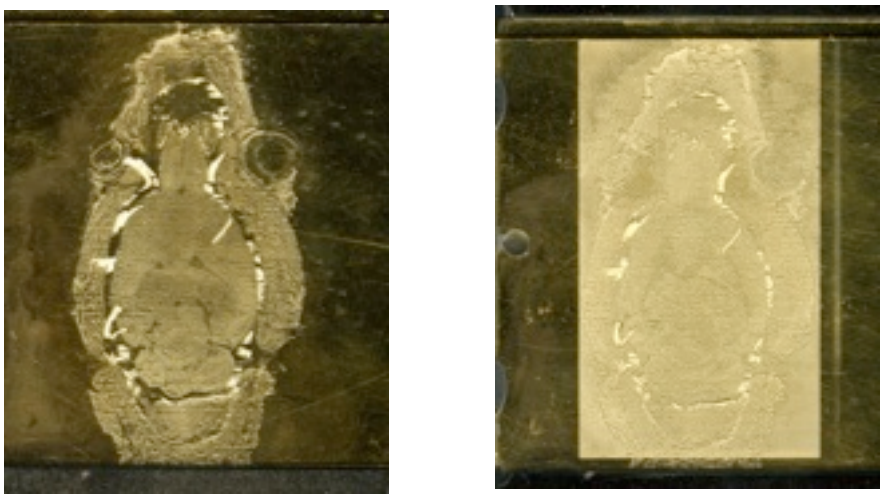

Figure 4. Photos of tissues on MALDI plate before and after spotting

across a region encompassing the rat brain, with a spectral dimension of 25203 and resulting in an average spectral resolution of approximately 1.5Da.

Co-registration

A well developed in-house registration method was used to co-register the different modalities together, generating a multi-modal dataset for correlation analysis. By aligning and concatenating the individual blockface images, a blockface volume was created and used as an intermediate reference frame to register MALDI data with MR volumetric data.

The high resolution 3D MR dataset was manually co-registered to the blockface volume using a six degree-of-freedom rigid transform. This intrinsically aligned the quantitative MR parametric maps (M0, T1, and T2) to the blockface volume

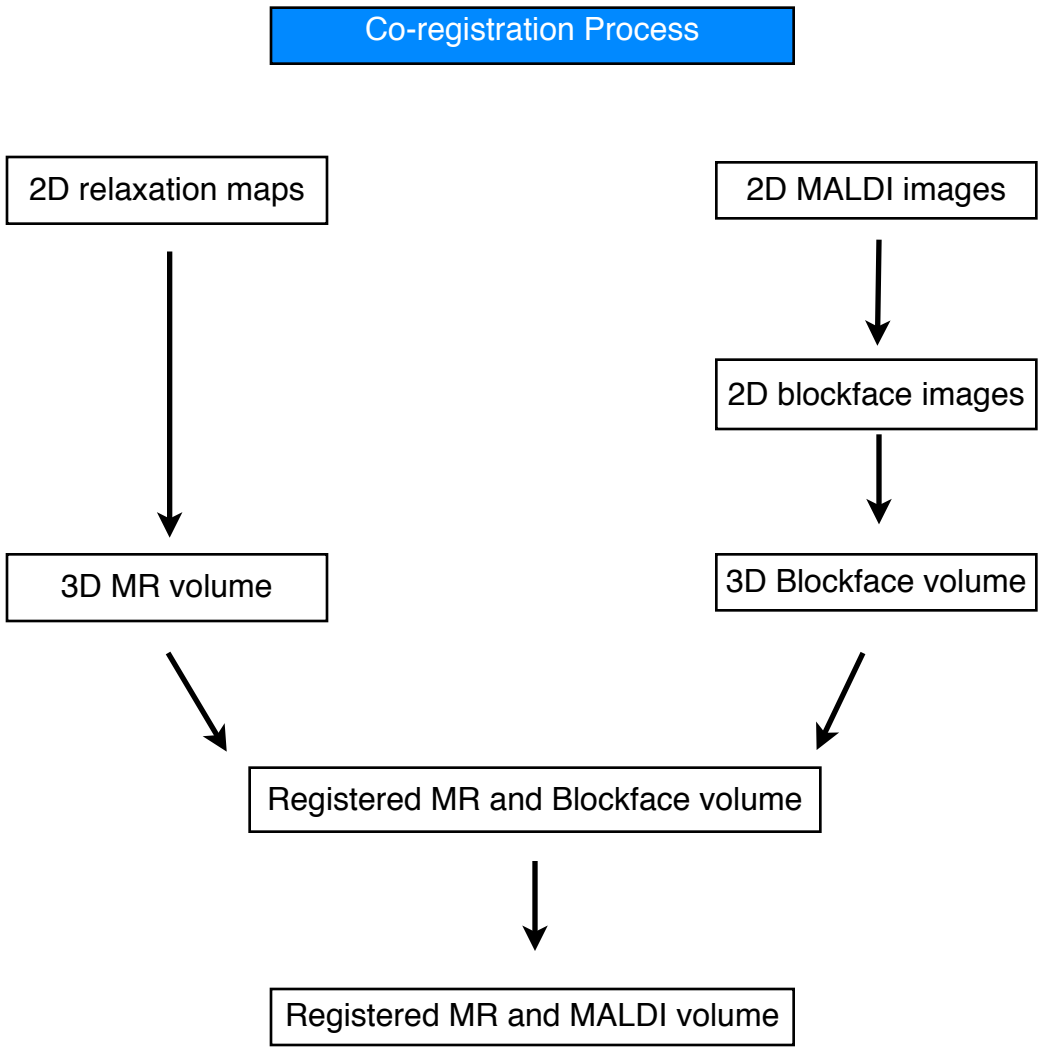

Figure 5 Work flow of co-registration between MR datasets and MALDI datasets using blockface volume as an intermediate.

since the weighted scans and 3D images were acquired in a single session. MALDI Images were also aligned manually to their corresponding blockface images, which placed them within the 3D reference frame of the blockface volume and the co-registered MR data. A diagram of co-registration workflow is shown in Figure 5.

Correlation Analysis

MALDI data were pre-processed before correlation analysis to reduce dimensionality and provide for a more computationally tractable dataset. The spectra in each MALDI IMS dataset were baseline corrected and aligned using the MATLAB functions msbackadj and msalign. Peaks were selected based on the derivative information obtained using a finite-difference approximation method. Peaks with less than 5 counts were filtered out as noise, leaving between 300-500 peaks of interest, which comprise approximately 91% of the total signal energy in the unfiltered data[1]. The filtered mass spectra were then subject to a principal component analysis to determine significant (orthogonal) modes of variation, by calculating a covariance matrix using the filtered mass spectra that decomposed using single value decomposition (SVD) methods. The resulting eigenvalues and eigenvectors represented the variance contribution of each mode and the peak-by-peak variation of each mode, respectively. We have re-termed the eigenvectors as eigenspectra to highlight their relationship with the original mean mass spectrum. That is, each eigenspectra represents the peak-by-peak change in peak intensity when compared to the mean mass spectra for a given MALDI IMS dataset. Eigenimages, which represent the spatial distribution of each eigenspectra, were also calculated as the dot-product of each eigenspectra with the filtered MALDI IMS data.

[1] This value was calculated by dividing the integrated area of the filtered peaks in the mean mass spectrum by the integrated area of the mean mass spectrum.

After we generated the eigenimages, we visually examined the contrast changes in each of them. The goal was to find the contrast patterns of specific areas that continually shown up consistently in all sections. We presumed that these patterns to correlate with specific protein profile changes that were similar across each section. Due to the intrinsic properties of the PCA method, where derived eigenvectors could be in opposing directions, the contrast patterns we seen in eigenimages could be reversed for different sections. The reason for this is because the direction of the first eigenvector need not be consistent for the SVD of each section. Thus, reflected directions would result in an orthogonal basis set where the eigenvectors (i.e. eigenspectra) that appear to be mirror images of each other. The true variation from the mean was identified by selecting a single protein within the identified protein profile, and examining its spatial distribution. Where the spatial distribution of the single protein matched the distribution of the eigenimage, we preserved the original eigenspectra. Where the single protein image demonstrated reversed contrast relative to the eigenimage, we assumed the eigenspectra was reflected about the origin. This method of protein profile identification was used for two reasons: 1) it greatly simplified the process of identifying candidate proteins, and 2) it provided a method to render disparate eigenspectra into a set of coherent protein profiles that could be examined in light of corresponding MR data.

After we found those eigenimages with protein variation patterns, we examined the correlation for the MR parametric maps against them. We manually delineated out the regions of interest that show the interesting patterns of

contrast using in-house developed MATLAB scripts. Pearson's correlation coefficient, r, which measures the linear dependence of the two sample, were calculated (using MATLAB functions corrf) against selective eigenimages with identified patterns of protein variations for the parametric MR measurements in the ROIs respectively, where

$$r = \frac{\sum_{i=1}^{n}(X_i - \overline{X})(Y_i - \overline{Y})}{\sqrt{\sum_{i=1}^{n}(X_i - \overline{X})^2}\sqrt{\sum_{i=1}^{n}(Y_i - \overline{Y})^2}} \qquad \text{(Equation 14)}$$

$\overline{X}$ and $\overline{Y}$ are the mean value for sample X_i and Y_i . A comparison of correlation before and after M0 correction was employed to verify the theoretically assumed relationship between relaxation measurements and proteomic measurements, where we compared the ratio of r values for correlations before M0 correction and after M0 correction with ratio value 1. If the ratio is less than 1, the r value of correlation before M0 correction is smaller than the correlation after the correction, which means the M0 correction strengthened the correlations.

$$\frac{r\_R1(R2)}{r\_M0R1(R2)} < 1 \qquad \text{(Equation 15)}$$

Results and discussion

We successfully acquired quantitative MR parametric maps and detailed macromolecular information for 3 sections of a control rat. Representative M0,

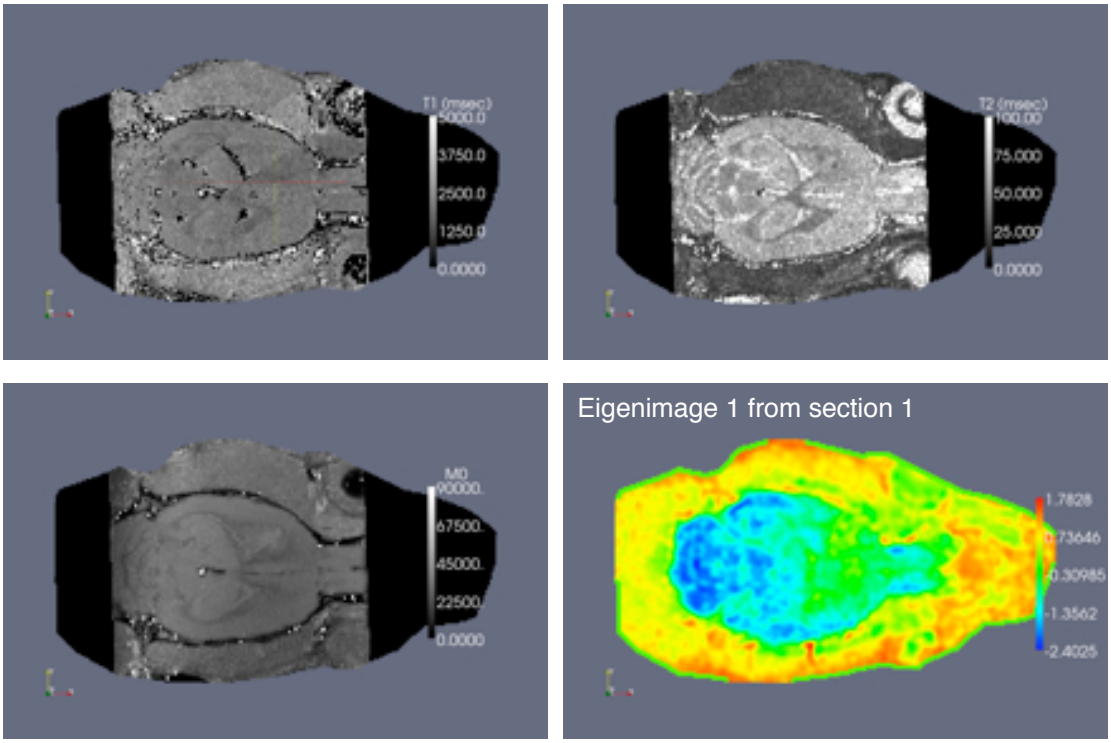

Figure 6. Quantitative M0, T1, T2 maps and a representative eigenimage. This Eigenimage 1 was generated from original MALDI image for section 1 of the rat head.

T1 and T2 parametric maps with a selected eigenimage derived from original M ALDI data for an single section of the rat head are shown in Figure 6. After co-registration, the parametric maps lined up well with the eigenimages.

Eigenimages generated from original MALDI images represent different groups of significantly varied proteins within the tissue. Contrast seen in eigenimages are inherently manipulated by those groups of varied proteins. Visually comparing these eigenimages from different sections we found that there were consistent tissue contrast patterns across sections. For example, for eigenimage 2 (Figure 7 group 1), it could be seen that muscle areas are brighter in section 1 and 3, whereas darker in section 5, compared with other tissues inside the brain

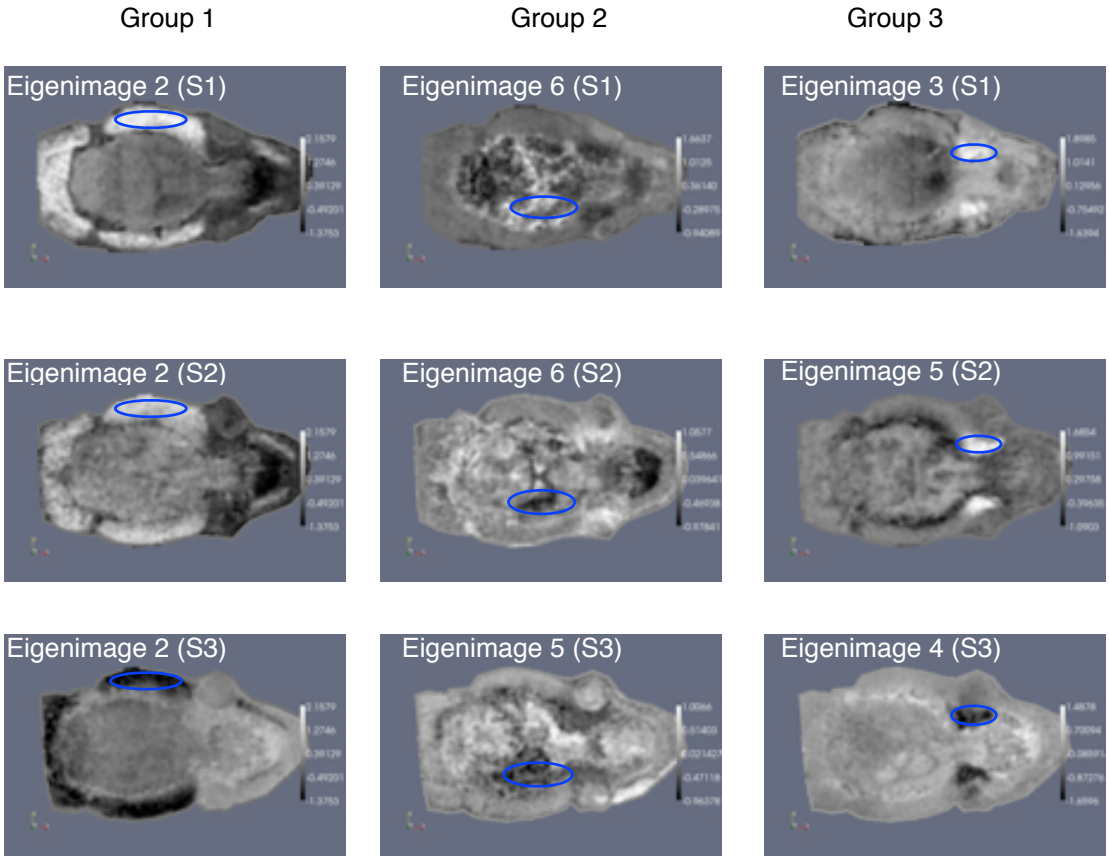

Figure 7. Groups of eigenimages used to derive the patterns of protein variation. Group 1: (top to bottom) Eigenimage 2 in section 1, 2, 3. Group 2 : (top to bottom) Eigenimage 6 in section 1, Eigenimage 6 in section 2 and Eigenimage 3 in section 5. Group 3 : (top to bottom) Eigenimage 3 in section 1, Eigenimage 5 in sectioin 2, Eigenimage 4 in section 3. Areas of interest are delineated in blue circle. The muscle tissue of interest in group 1 exhibits the contrast change of “bright-bright-dark” across sections, compared with tissue inside the skull. The whitematter tissue of interest in group 2 shows the pattern of “bright-dark-dark” across sections compared with other areas of tissues in the brain. Tissue of interest around eyeball area in group 3 shows the pattern of “bright-bright-dark” across sections.

(Figure 7). For all 3 sections, the muscle area in eigenimge 2 were therefore “h ighlighted”, which means there are certain group of proteins behind the eigenimage 2 that contribute a lot to the variations in proteomic measurements of muscle. For the “reversed” contrast seen in eigenimage 2 of section 3 for the muscle areas, it is probably because the eigenvectors used to generated eigenimage 2 of section 3 pointed at the opposite direction compared with the

direction that eigenvectors of eigenimage 2 in section 1 and 2 pointed at. We compared the eigenspectras (eigenvectors) behind the eigenimage 2 in all 3 sections (Figure 8) and found out that the peaks in these eigenspectras lined up well but the eigenspectra from section 3 looked mirrored compared with eigenspectras from section 1 and 2.

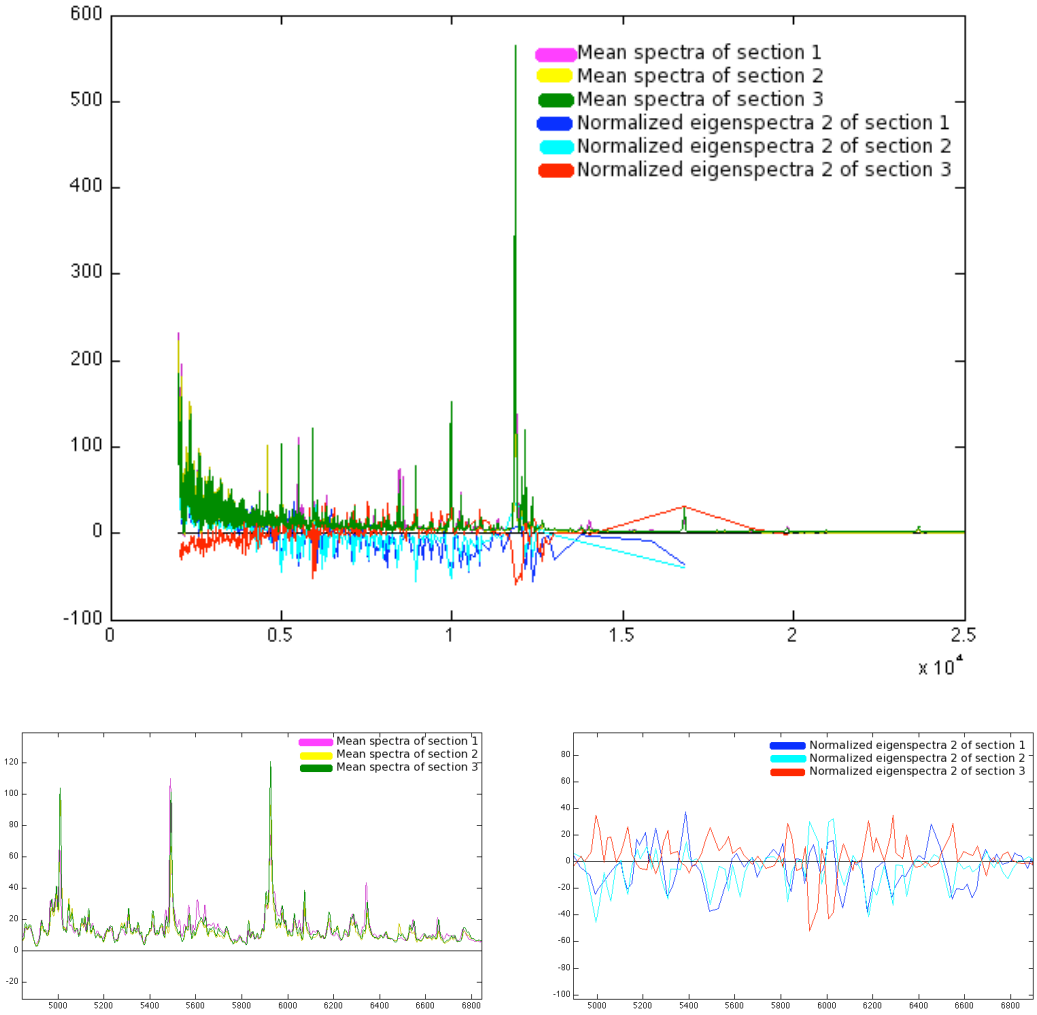

Figure 8. Comparison of mean mass spectra for all 3 sections and normalized eigenspectra 2 for all 3 sections. Mean mass spectra from all 3 sections lined up well with each other. Normalized eigenspectra 2 of section 3 showed the reverse pattern of change compared with section 1 and section 2.

This result demonstrate our assumption of the “contrast reversal ” in the muscle areas in eigenimage 2 of section 3. Therefore, If the peaks for a certain mass-to-charge ratio in eigenpectras from section 1,2 and 3 showed the pattern of “negative-negative-positive”, we preserved the corresponding mass-to-charge ratio. Based on this protocol, we found a group of proteins that has this pattern of changes in eigenspectra 2 across the three sections for the muscle tissue (see Tbl 1, group 1). The actual changes of amount across sections of these proteins were examined using the methods described in the previous section. Similarly other areas(Figure 7, group 2 and 3) ,in the brain near white matter tissue and near the eyes, also demonstrated similar contrast and protein variations across

Table 1. Groups of proteins and peptides identified for ROIs of muscle, whitematter and tissue around eye area and their changes relative to the mean across sections.

Group 1

MW (Da)	Changes
4350	↑
5007	↓
5923	↑
7726	↓
8456	↓
10260	↓
12140	↓

Group 2

MW (Da)	Changes
3607	↓
3783	↓
3839	↓
4752	↑
5007	↑
5044	↑
7038	↑
9669	↓
11840	↓

Group 3

MW (Da)	Changes
3551	↓
3607	↓
3783	↓
3839	↓
4529	↓
4638	↓
7157	↓
8456	↑

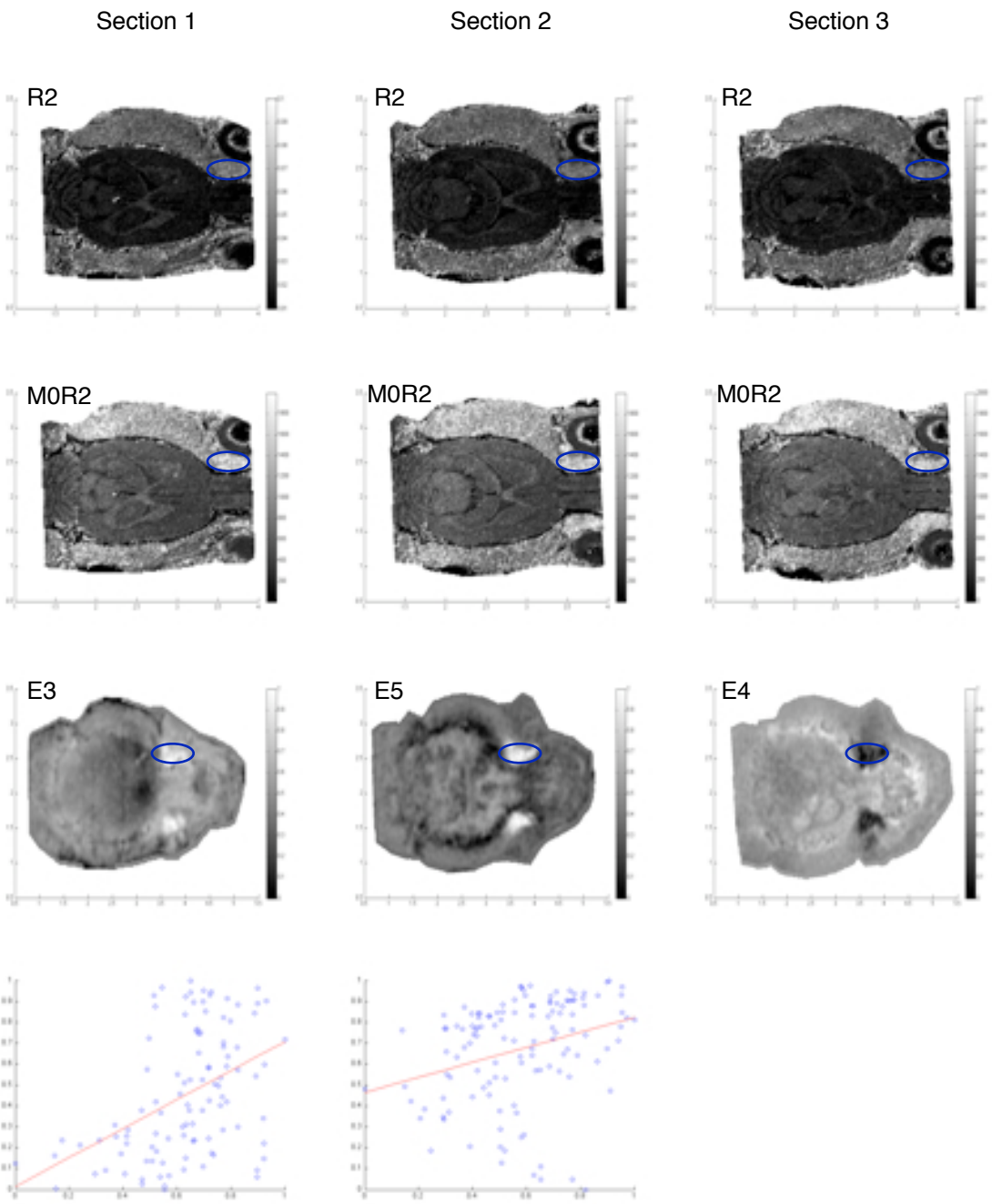

Figure 9. Correlation results for ROIs of tissue around the eye area of 3 sections respectively. First row are the R2 maps of each section. M0 corrected R2 maps for each section are shown in the second row. Third row shows the normalized selective eignimages in each section. The last row shows the scatter plot of the correlation. The red line in the scatter plot of the two datasets against each other is the fitted linear regression between normalized R2 and the eigenimage for each section. The outlier points were identified using Grubb's test and filtered out in the scatter plot. For tissues selected here around the eye in section 3, we were unable to get significant correlations between MR parametric maps and the eigenimage 4.

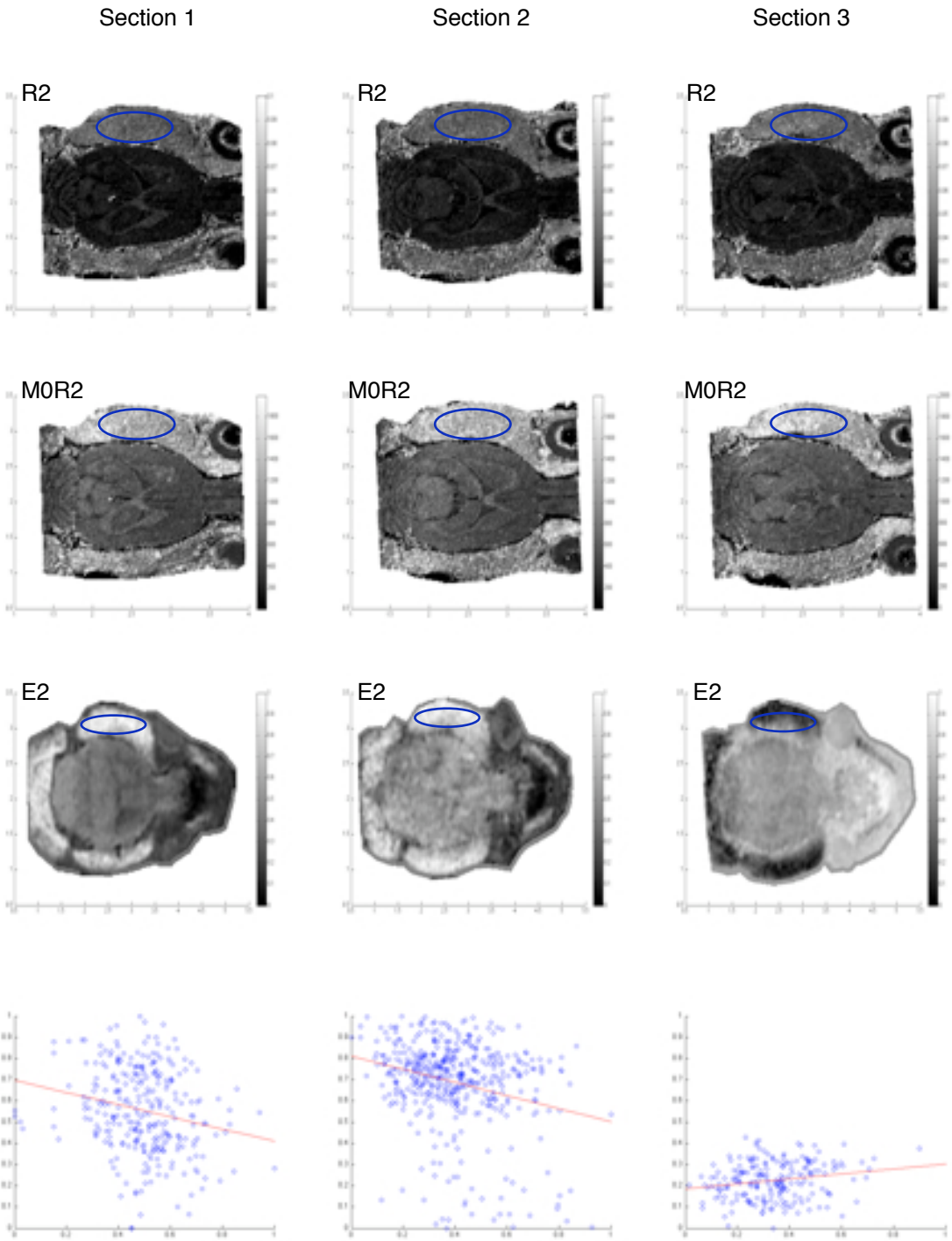

Figure 10. Correlation results for ROIs of muscle for 3 sections respectively. First row are the R2 maps of each section. Second row are M0 corrected R2 maps for each section. Third row shows the normalized eignimages used in each section. The last row shows the scatter plot of the correlation. The red line in the scatter plot of the two datasets against each other is the fitted linear regression between normalized R2 and the eigenimage for each section. The outlier points were identified using Grubb's test and filtered out in the scatter plot.

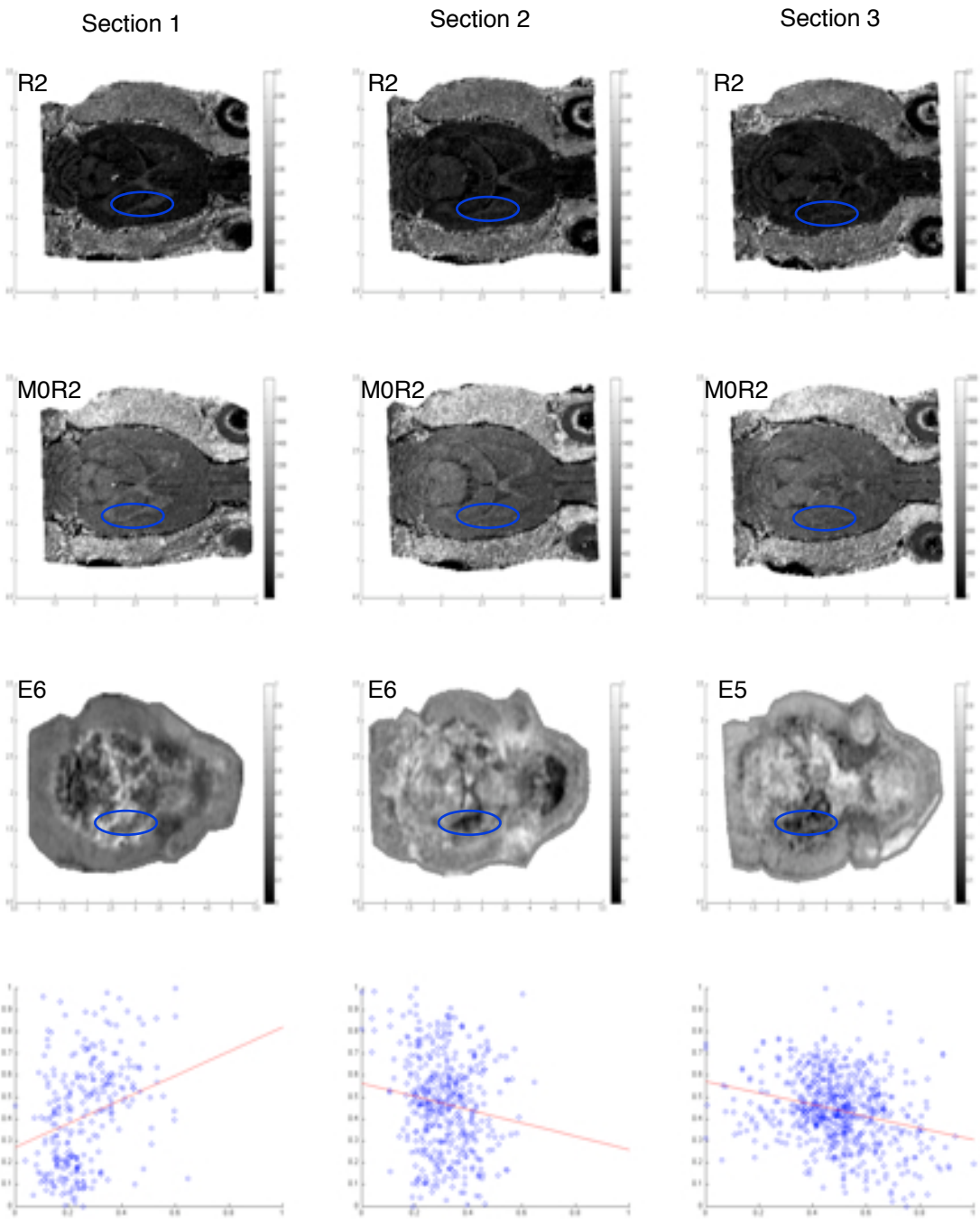

Figure 11. Correlation results for whitematter ROIs of 3 sections respectively. First row are the R2 maps for each section. M0 corrected R2 maps for each section are shown in the second row. Third row shows the normalized selective eignimages in each section. The last row shows the scatter plot of the correlation. The red line in the scatter plot of the two datasets against each other is the fitted linear regression between normalized R2 and the eigenimage for each section. The outlier points were identified using Grubb's test and filtered out in the scatter plot.

sections (see Tbl 1, groups 2 and 3). We hypothesized that these groups of proteins may potentially responsible for the variations in proteomic measurements of those areas we found above. We also hypothesized that the variations seen in quantitative MR parametric maps within the same areas could be correlated with these pattens of protein variations. To testify our hypothesis, correlation analysis between MR parametric maps and those eigenimages with identified group of proteins were performed for the 3 ROIs in all 3 sections. The results are shown in figure 9, 10 and 11 respectively. Correlation between M0 corrected relaxation maps and these eigenimages within the same areas were also examined, as shown in Figure 12, 13 and 14. Significant correlations were found between R2 relaxation maps and the selected eigenimages, and therefore, the identified patterns of protein changes. However, we were unable to achieve robust correlations between R1 relaxation maps and these selected eigenimages, probably due to the lower signal-to-noise ratio in R1 relaxation maps. We were also unable to get significant correlations between MR parametric maps and eigenimage 4 for ROIs of tissue around the eye at section 3 (Figure 11). It may due to the less tissue collected in that area compared with the former 2 sections. Therefore, the MALDI signals of the group of proteins at that area are very weak.

From figure 12, 13 and 14, it can be seen that after M0 correction, the correlation between R2 relaxation maps and the eigenimages get strengthened. This result matches with our previous hypothesis that taking the total water

content factor into account will improve the correlation between relaxation measurements and the protein profile.

	Without M0 Correction	With M0 correction
S1	3.15E-01	3.39E-01
S2	1.50E-01	1.96E-01
S3	1.39E-01	1.47E-01

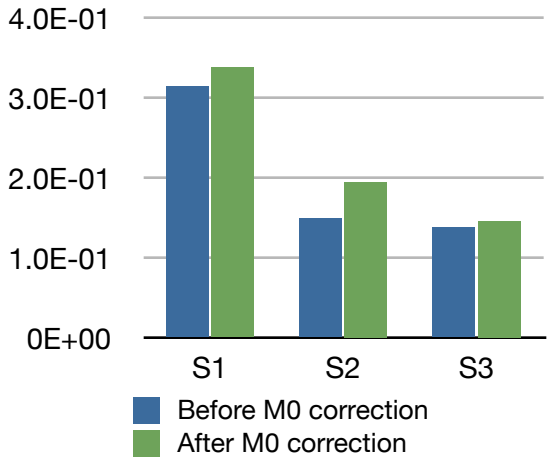

Figure 12. Interslices comparison of correlation results before and after M0 correction in ROIs of whitematter

	Without M0 Correction	With M0 correction
S1	2.15E-01	2.37E-01
S2	2.63E-01	2.67E-01
S3	1.71E-01	2.23E-01

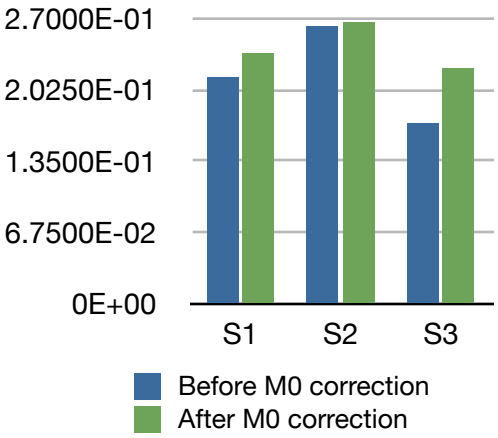

Figure 13. Interslices comparison of correlation results before and after M0 correction in ROIs of muscle

	Without M0 Correction	With M0 correction
S1	4.39E-01	4.95E-01
S2	3.05E-01	3.21E-01

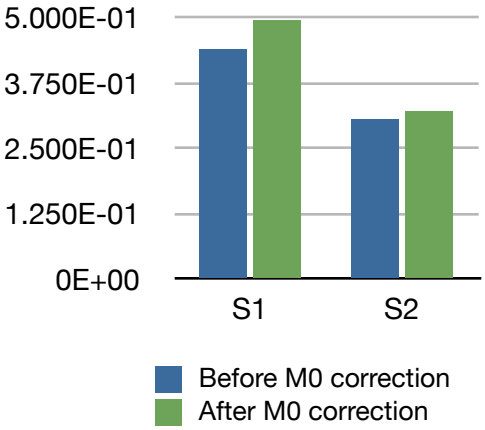

Figure 14. Interslices comparison of correlation results before and after M0 correction in ROIs of tissue around the eye

CHAPTER II

CONCLUSIONS

For now, we have been able to develop protocols to generate high resolution quantitative MR parameter maps of M0,T1 and T2 for the rat head. We also acquired corresponding detailed tissue macromolecular composition and concentration information using MALDI IMS technique. Using our well developed in-house co-registration methods, we were able to register these two data modalities together which makes the correlation analysis possible. On the MALDI side, we successfully decomposed and generated 20 eigenimages from the original MALDI measurements using PCA method. Analysis on these eigenimages allowed us to investigate proteomic variation in specific areas of the rat head in terms of different patterns of changes in groups of proteins. For muscle, selected whitematter and tissue around eye areas, we derived protein variation patterns for each of them from those eigenimages and examined the correlations against corresponding MR relaxation measurements in the same areas.

Our correlation results for these areas of interest demonstrated the correlations between variations in MR relaxation properties and corresponding patterns of protein changes in MALDI measures. The correlation results before and after M0 correction demonstrate our hypothesis that when total water content is taken into

account for correlating tissue MR relaxation measurements with tissue macromolecular content, the correlation will be strengthened.

Due to the lower signal-to-noise ratio in longitudinal relaxation maps, we were unable to achieve robust correlations between R1 relaxation rate measurements and corresponding detailed protein expressions. The tissue loss during the tissue transferring process could be another potential reason for the poor correlation. The lower sensitivity of MALDI in higher range of molecular weights prevented us from getting identifications of proteins at a wider range.

To our knowledge, it is the first time to combine relaxation measurements with detailed proteomic information to investigate whether variations in MRI properties can be explained by changes in pattern of proteins expressed in different tissues. Our current results provided initial support to our theoretical hypothesize that variations seen in MR properties could be correlated with corresponding macromolecular changes in tissue. In the future work, we aim to refine our MR protocols to get higher resolution parametric maps without compromising the signal-to-noise ratio. Also, Methods are expected to be developed to expand the range of mass to charge ratio where more proteins and peptides in tissue could be identified using MALDI IMS technique. More animals will be employed to test the robustness of our experimental results. New sights yield from the correlation analysis will not only enrich the interpretation of both modalities' data but also aid in understanding the mechanism that why MR signals acquired are different in heterogeneous tissue.

REFERENCE

1. Hawkes RC, Holland GN, Moore WS, et al: Nuclear magnetic resonance tomography of the brain: A preliminary clinical assessment with demonstration of pathology. J Comput Assist Tomogr 4: 577-586,1980.

2. Brant-Zawadzki M, Davis PL, Crooks LE, et al: NMR demonstration of cerebral abnormalities: Comparison with CT. AJR 140: 847-854,1983

3. Zimmerman RD, Bilaniuk LT, Goldberg HL, et al: Cerebral nuclear magnetic resonance imaging : Early results with a 0.12T resistive system. AJR 141: 1187-1193,1983

4. Fletcher BD, Jacobstein MD, Nelson AD, Rimmelschneider TA, Alfidi RJ. Gated magnetic resonance imaging of congenital cardiac malformations. Radiology 150: 137-140,1984.

5. Dider D., Higgins C.B., Fisher M.R., Osaki L., Silverman N.M.,Cheitlin M.D. Congenital heart disease : gated MR imaging in 72 patients. Radiology 1986;158:227-235

6. Higgins C.B., Byrd B.F., Farmer D.W., Osaki L., Silverman N.H., Cheitlin M.D. Magnetic resonance imaging in patients with congenital heart disease. Circulation 1984;70:851-860

7. Bloem J.L., Falke T.H.M., Taminiau A.H.M., et al:MRI of primary malignant bone tumors. Radiographics, 1985; 5:853-886.

8. Lamir A., Hadar H., Cohen I., et al: Gaucher disease: assessment with MR imaging. Radiology 1986;161:239

9. Mickinstry C.S., Steiner R.E>, Young A.T., et al: Bone marrow in leukaemia and aplastic anemia: MR imaging before, during and after treatment. Radiology 1987;162:701-707

10. Abragam "Principles of Nuclear Magnetism" (Oxford University Press, 1961)

11. E.Mark Haacke, Robert W. Brown, Michael R. Thompson, Ramesh Venkatesan. Magnetic resonance imaging : Physical Principles and Sequence Design. 1999

12. S.H. Koenig, Cholesterol of myelin is the determinant of gray-white contrast in MRI of brain, Magn. Reson. Med. 20, 285 (1991).

13. Damon B.M., Gregory C.D., Hall K.L.,Stark H.J., Gulani V. And Dawson M.J. “Intracellular acidification and volume increases explain R(2) decreases in exercising muscle”. Magn Reson Med. 2002 Jan;47(1):14-23

14. Fenrich, F.R.E., C. Beaulieu, and P.S. Allen, *Relaxation times and microstructures.* Nmr in Biomedicine,2001. 14(2): p. 133-+.

15. Virta, A., M. Komu, and M. Kormano, *T1 of protein solutions at very low fields: Dependence on molecular weight, concentration, and structure.* Magnetic Resonance in Medicine, 1997. 37(1): p.53-57

16. Trupat K, Karas M, Hillenkamp F (1991). "2,5-Dihidroxybenzoic acid: a new matrix for laser desorption-ionization mass spectrometry". Int. J. Mass Spectrom. Ion Processes 72 (111): 89–102.

17. Chaurand P, Schwartz SA, Caprioli RM., Assessing protein patterns in disease using imaging mass spectrometry., J Proteome Res. 2004 Mar-Apr;3(2):245-52.

18. Stoeckli, M, Chaurand P, Hallahan DE and Caprioli RM Imaging mass spectrometry: a new technology for the analysis of protein expression in mammalian tissues Nature Medicine (2001) 7, 493-496

19. Chaurand, P.; Schwartz, S. A.; Caprioli, R. M. *J. Proteome Res.* 2004, *3*, 245-252

20. Troendle, F. J.; Reddick, C. D.; Yost, R. A. *J. Am. Soc. Mass Spectrom.* 1999, *10*, 1315-1321.

21. Reyzer, M. L.; Caldwell, R. L.; Dugger, T. C.; Forbes, J. T.; Ritter, C. A.; Guix, M.; Arteaga, C. L.; Caprioli, R. M. *Cancer Res.* 2004, *62*, 9093-9100.

22. Groseclose MR, Andersson M, Hardesty WM, Caprioli RM. Identification of proteins directly from tissue: in situ tryptic digestions coupled with imaging mass spectrometry. *Journal of Mass Spectrometry.* 2007, *42 (2)*: 254-262.

23. Khatib-Shahidi, S., Andersson, M., Herman, J.L., Gillespie, T.A., Caprioli, R.M. Direct molecular analysis of whole-body animal tissue sections by imaging MALDI mass spectrometry. *Analytical Chemistry.* 2006, *78(18)*: 6448-56.

24. Andersson, M., Groseclose, M.R., Deutch, A.Y, Caprioli, R.M. Imaging mass spectrometry of proteins and peptides: 3D volume reconstruction. . *Nature Methods.* 2008, *5(1)*: 101-8.

25. Aerni, H.R.; Cornett, D. S.; Caprioli, R. M. *Anal. Chem.* 2006, *78*, 827-834.

26. J.M.Fitzpatrick, J.B West, and C.R. Maurer, Jr. “Predicting error in rigid-body, point-based image registration”, Special issue of IEEE Trans. Medical Imaging on Image Registration 17, 694-702 (1998).

27. J.B. West and J.M. Fitzpatrick, “The distribution of target error in rigid-body, point-based registration”, IEEE Transactions on Medical Imaging 20,917-927 (2001).

28. J.B. West, J.M. Fitzpatrick, M.Y. Wang, B. M. Dawant, C. R. Maurer, Jr., R. M. Kessler, and R. J. Maciunas, “restrospective intermodality registration techniques:

surface-based vs. Volume-based", IEEE Transactions on Medical Imaging 18, 144-150 (1999).

29. Herring J. L. And Dawant B.M. "Automatic Lumbar Vertebral Identification Using Surface-based Registration" Journal of Biomedical Informatics, 34, 74-84,2001

30. Herline A.J., Herring J.L., Stefansic J.D., Chapman W.C., Galloway R.L., and Dawant B.M. "Surface registration for use in interactive image guided liver surgery", Computer Aided, Surgery, 5(1), pp. 11-17, 2-000

31. Herring J.L, Dawant B.M., Maurer C.R. Et al. "Surface-based registration of CT images to physical space for image-guided surgery of the spine: a sensitivity study", IEEE Transactions on Medical Imaging, 17(5),pp 743-752,1998

32. Maurer C.R., Aboutanos G.B., Dawant B.M., Margolin R.A., Maciunas R.J., and Fitzpatrick J.M. "Registration of CT and MR brain images using a combination of points and surfaces", IEEE Transactions on Medical Imaging, pp. 836-849,1996.

33. Dawant B.M., Hartmann S.L., Thirion J-P., Maes F., Vandermeulen D., and Demaerel P. "Automatic 3D segmentation of internal structures of the head in MR images using a combination of similarity and free form transformations: Part I, methods and validation on normal subjects", IEEE Transactions on Medical Imaging, 18(10), pp. 897-908, 1999.

34. Hartmann S.L., Parks M.H.,Martin P.R. And Dawant B.M., "Automatic 3D segmentation of internal structures of the head in MR images using a combination of similarity and free form transformations : Part II, validation on severely atrophied brains", IEEE Tran. Med Imaging, 18(10), pp. 917-926,1999.

35. Rohde, G.K., Aldroubi A, and Dawant B.M. "The adaptive bases algorithm for intensity based nonrigid image registration ", IEEE Transactions on Medical Imaging. 2003

36. Dawant B.M.,Hartmann S.L., Shiyan Pan, and Gadamsetty S. "Brain atlas deformation in the presence of large space-occupying lesions", Jounal of Computer Aided Surgery, 7(1),pp.1-11,2002.

37. Bert G, Peter. P. D., Herman S. "Rat C6 glioma as experimental model system for the study of glioblastoma growth and invasion".

38. Tuhin K S, Sheerin K.S, John C.G. et. al. "Integrating spatially resolved three-dimensional MALDI IMS with in vivo magnetic resonance imaging". Nature Methods - 5, 57 - 59 (2007)